MODELING OF POROSITY FORMATION
AND FEEDING FLOW IN STEEL CASTING

Kent D. Carlson, Zhiping Lin, Richard A. Hardin and Christoph Beckermann

Department of Mechanical and Industrial Engineering
The University of Iowa
Iowa City, Iowa 52242

Abstract

A multi-phase model is presented that predicts melt pressure, feeding flow, and porosity formation and growth in steel castings during solidification. By combining Darcy's law, which governs fluid flow in the mushy zone, with the equation for Stokes' flow, which governs the motion of slow-flowing pure liquid, it is possible to derive a momentum equation that is valid everywhere in the solution domain. A pressure equation is then derived by combining this momentum equation with a continuity equation that accounts for the solid, liquid and gas phases present. The partial pressures of the gas species dissolved in the melt are determined using the species concentrations, which are found by solving a species conservation equation for each gas species present. This species equation accounts for macrosegregation of gas species due to the flow. Once the total gas pressure is high enough to cause pore nucleation, the amount of porosity that forms is determined from the continuity equation. This multi-phase model has been successfully implemented in a general-purpose casting simulation code. Results are presented to illustrate the basic physical phenomena involved. For two of the examples provided, the predicted porosity distributions are compared to radiographs of steel castings produced in sand molds. Good agreement is found between simulation and casting results. An appendix is included that describes preliminary work on another defect modeling project involving reoxidation inclusions.

Introduction

Porosity-related defects are a major cause of casting rejection and re-work in the casting industry. Porosity ranges in size from microporosity, such as micron-sized gas bubbles, to macroporosity, such as millimeter- to centimeter-sized centerline shrinkage porosity, or even larger shrinkage cavities found in inadequately fed cast sections. Microporosity can cause leaks in fluid-containing vessels or reduce mechanical properties such as fatigue life, while macroporosity can cause structural unsoundness and rapid failure. Porosity-related defects come about due to the interplay of several phenomena that occur during solidification. As the melt cools, the solubility of gases dissolved in the melt decreases. If the solubility limit is reached, gas will precipitate out of the melt. In addition, gases are much less soluble in solid than in liquid, and hence gas is rejected from the solid to the liquid during solidification, which increases gas levels in the remaining liquid. Finally, the pressure gradient associated with metal flowing through the mushy zone to feed solidification shrinkage decreases the pressure in the casting, which further lowers the solubility. Even in the absence of dissolved gases, pores can form solely due to shrinkage. If porosity precipitates early in solidification, it can form as spherical bubbles (i.e., gas porosity). If pores precipitate later in solidification, they are constrained by the existing dendritic network and take on an irregular shape.

Porosity formation during cast alloy solidification has been investigated by many researchers, dating back to the early 1-D microporosity modeling work of Piwonka and Flemings [1]. The seminal work on microporosity modeling in (2-D) shaped castings was performed by Kubo and Pehlke [2]. In the years since the work described in [2], many researchers have refined and advanced this work, and several other modeling approaches have also been attempted. An extensive review of the research in this area is provided by Lee et al. [3]. More recently, Sabau and Viswanathan [4] provide a 3-D model for microporosity prediction in hydrogen-aluminum alloy systems, that augments a microporosity prediction model with the ability to compute shrinkage porosity when feeding flow is cut off. Their model computes flow and pressure both in the liquid region and in the mushy zone. When feeding flow to a region is cut off, they no longer solve for pressure or velocity in the region, but rather compute porosity such that it compensates for all the shrinkage occurring in that region. Another recent 3-D model is presented by Pequet et al. [5]. Their approach couples a microporosity model with macroporosity and shrinkage pipe predictions. They only apply their microporosity model in the mushy zone. They incorporate this into casting solidification simulation by superimposing a fine finite volume grid onto the coarser finite element mesh used for heat flow computations. They solve the governing equations of microporosity formation in the mushy zone, and impose boundary conditions around this zone. To determine the boundary conditions, they must decide if each liquid region of the casting is connected to a free surface, surrounded by solid or surrounded by a mushy zone. In the latter two cases, integral boundary conditions must be solved to determine the pressure boundary condition. Due to inaccuracies in this computation,

the void fractions are adjusted to ensure global mass conservation.

The present 3-D approach uses a single-domain model to determine pressure, feeding flow, microporosity, macroporosity, and shrinkage cavities throughout a shaped casting as it solidifies. The model is presented in the next section, and applications are presented in the subsequent section. Another defect modeling project currently underway involves predicting the formation, growth and motion of reoxidation inclusions during steel casting. Project details and preliminary inclusion modeling results are provided in the Appendix.

Model Description

The present multi-phase model assumes that each volume element in the casting is composed of some combination of solid metal (s), liquid metal (l), porosity (p), and air (a), such that the volume fractions satisfy $\varepsilon_s + \varepsilon_l + \varepsilon_p + \varepsilon_a = 1$. Mixture properties are obtained as the sum of the property values for each phase multiplied by their respective volume fractions. For example, the mixture density is given by: $\rho = \varepsilon_s \rho_s + \varepsilon_l \rho_l + \varepsilon_p \rho_p + \varepsilon_a \rho_a$.

Mixture Energy Conservation. The energy conservation equation can be written as

$$\left(\rho c - \rho L \frac{d\varepsilon_s}{dT} \right) \frac{\partial T}{\partial t} = \nabla \cdot \left(\lambda \nabla T \right) \tag{1}$$

where L is the latent heat per unit mass, ρc is the mixture thermal capacitance, and λ is the mixture thermal conductivity. The solid fraction, ε_s, is assumed to be a known function of temperature. When the liquid fraction approaches zero, the latent heat term is set to zero even if the temperature is still above the solidus. Eq. (1) neglects the advection of heat due to the feeding flow; this term can be important at riser necks, where the maximum velocities occur. A future version of the model will include this term.

Mixture Mass Conservation. The mixture continuity equation is simplified by subtracting out the continuity equation for the air phase (i.e., $\partial(\varepsilon_a \rho_a)/\partial t + \nabla \cdot (\varepsilon_a \rho_a \mathbf{v}_a) = 0$), in order to avoid calculation of the unknown air velocity, $\mathbf{v}_a$. The solid metal and the porosity are assumed to be stationary. Then,

$$\frac{\partial}{\partial t} \left(\varepsilon_s \rho_s + \varepsilon_l \rho_l + \varepsilon_p \rho_p \right) + \nabla \cdot \left(\rho_l \mathbf{v} \right) = 0 \tag{2}$$

or

$$\nabla \cdot \mathbf{v} = -\frac{1}{\rho_l} \left[\frac{\partial}{\partial t} \left[\varepsilon_s (\rho_s - \rho_l) + \rho_l - \varepsilon_p (\rho_l - \rho_p) \right] + \mathbf{v} \cdot \nabla \rho_l \right] = CRHS \tag{3}$$

where $\mathbf{v}$ denotes the superficial liquid velocity, $\mathbf{v} = \varepsilon_l \mathbf{v}_l$. Eq. (3) shows that the divergence of the velocity field is a function of the solidification contraction, liquid density change, porosity evolution, and gradients in the liquid density (although this last contribution is quite small).

Liquid Momentum Conservation. The feeding velocities in the casting are determined from

$$\nabla^2 \mathbf{v} = \frac{\varepsilon_l}{K} \mathbf{v} + \frac{\varepsilon_l}{\mu_l} \nabla P - \frac{\varepsilon_l}{\mu_l} \rho_{ref} \mathbf{g} \qquad (4)$$

where P is the melt pressure, μ_l is the dynamic viscosity of the liquid (assumed to be constant), $\mathbf{g}$ is the gravity vector, and ρ_{ref} is the reference liquid density, taken as the melt density at the liquidus temperature. Buoyancy induced flow is neglected. The permeability, K, is given by $K = K_r K_0 \left(1 - \varepsilon_s - \varepsilon_g\right)^3 / \left(\varepsilon_s + \varepsilon_g\right)^2$, where $K_0 = 6 \times 10^{-4} \lambda_1^2$, in which λ_1 is the primary dendrite arm spacing, and $K_r = \varepsilon_l / \left(\varepsilon_l + \varepsilon_a\right)$ is the relative permeability for two-phase (liquid plus air) flow in porous media [6]. In the present study, a constant value of $\lambda_1 = 143$ μm was used. Due to the small Reynolds number of the feeding flow, the inertial terms have been neglected in the momentum equation. Notice that Eq. (4) reduces to Stokes' equation when K approaches infinity, which occurs in the single-phase liquid region. Also recognize that, in the mushy zone, the left-hand side of Eq. (4) becomes very small relative to the permeability term, and the equation then reduces to Darcy's law.

Melt Pressure. By manipulating and combining Eq. (3) and Eq. (4), it is possible to derive the following equation for the melt pressure, P:

$$\nabla \cdot \left(\frac{K}{\mu_l} \nabla P \right) = -\left(CRHS\right) + \nabla \cdot \left(\frac{K}{\mu_l} \rho_{ref} \mathbf{g} \right) + \nabla \cdot \left(\frac{K}{\varepsilon_l} \nabla^2 \mathbf{v} \right) \qquad (5)$$

where $CRHS$ is the right-hand side of Eq. (3). The last two terms on the right-hand side of Eq. (5) are very small, and actually vanish for a constant ε_l (note that $\nabla \cdot \nabla^2 \mathbf{v} = 0$ always). Thus, Eq. (5) is only weakly coupled with Eq. (4).

Gas Species Conservation. The concentration of each gas species dissolved in the melt, C_l (in weight fraction), is obtained from the mixture species conservation equation. For simplicity, consider the case of only one dissolved gas species in the melt; the present study uses nitrogen. Realizing that $C_a = 0$, we have

$$\frac{\partial}{\partial t} \left(\varepsilon_s \rho_s C_s + \varepsilon_l \rho_l C_l + \varepsilon_p \rho_p C_p \right) + \nabla \cdot \left(\rho_l C_l \mathbf{v} \right) = 0 \qquad (6)$$

Assuming complete mixing of gas species within each phase in a volume element, the

concentration of gas in the solid is given by $C_s = \kappa C_l$, where κ is the partition coefficient. The concentration of gas in the pores is unity (i.e., $C_p = 1$), because if only one gas species is present, then all porosity is composed of this gas. If multiple gas species are present, C_p can be found for each gas using thermodynamic relations. To the best of the authors' collective knowledge, no one has previously included the last term on the left-hand side of Eq. (6), which accounts for advection of the gas species due to feeding flow.

Pore Pressure. Knowing C_l from Eq. (6), it is possible to determine the partial pressure of the gas in the pores from Sievert's law as

$$P_p = \left[100\, C_l \left(\frac{f}{K_e} \right) \right]^2 \times 101{,}325 \tag{7}$$

where the value 100 converts C_l from wt fraction to wt pct, and the value 101,325 converts the pressure from atm to Pa. In Eq. (7), $f = f(T)$ and $K_e = K_e(T)$ are the activity and equilibrium coefficients of the gas species present, respectively. In the present work, the activity coefficient is taken as a constant, $f = 1$, and the expression used for the equilibrium coefficient is $\log(K_e) = -a/T - b$, where $a = 188.1$ K and $b = 1.246$ for nitrogen.

Porosity Formation. The governing equations listed above are solved to give the melt pressure, P, pore pressure, P_p, and feeding velocity, $\mathbf{v}$, throughout the casting. Porosity is assumed to nucleate if

$$P \le P_p - 2\sigma / r \tag{8}$$

The last term in Eq. (8) is the capillary pressure due to surface tension, where σ is the surface tension and r is the radius of the forming porosity (this term assumes the pores are spherical). For the results presented here, the capillary pressure is set to zero for simplicity. If the capillary pressure is not neglected, a separate model must be specified for the pore number density or radius evolution. When porosity forms, the melt pressure at that location is forced using the equality in Eq. (8); i.e., $P = P_p - 2\sigma / r$. This allows the continuity equation, Eq. (2), to be solved for the pore fraction, ε_p. Note that in regions that are completely surrounded by solid, forcing the melt pressure during pore formation using $P = P_p - 2\sigma / r$ ensures that the pressure does not float arbitrarily. Once the pore fraction is known, the liquid fraction is updated according to $\varepsilon_l = 1 - \varepsilon_p - \varepsilon_s - \varepsilon_a$.

Open Shrinkage Pipe Formation. A special procedure is needed to simulate the formation of a riser pipe that is open to the atmosphere. In those volume elements that are emptying of liquid,

the pressure is forced to atmospheric pressure, P_{atm}. Then, the continuity equation, Eq. (2), is solved for the liquid fraction, ε_l, while keeping ε_p constant (i.e., no pore formation or growth when air is present). Finally, the air fraction is obtained from $\varepsilon_a = 1 - \varepsilon_p - \varepsilon_s - \varepsilon_l$.

Applications

The present model has been implemented in the general-purpose casting simulation software package MAGMASOFT [7]. The applications presented in this section were simulated using property data generated with the program IDS [8] for AISI 1022 steel with dissolved nitrogen; this includes temperature-dependent partition coefficient (κ) data for nitrogen. The gas density was calculated using the ideal gas law. The mold properties were obtained from an available database for furan sand. The initial nitrogen concentration in the melt was set to 0.0001 wt fraction, or 100 ppm.

Plate with Hot Spot

The first application is a simulation of a simple end-risered 3"T x 6"W x 28.5"L plate with a 5-2/3"T x 6"W x 6"L block of metal on the end opposite the riser, which creates a hot spot at the end of the plate. The riser has a diameter of 6", and a height of 8". The geometry is shown in Fig. 1. The simulation was performed without filling, with an initial melt temperature of 2840°F. As the casting begins to solidify, the pressure in the plate drops from the riser to the hot spot, and feed metal flows from the riser, down the plate, into the hot spot to feed the shrinkage. As solidification progresses, feeding becomes more difficult and the pressure drop increases. This can be seen in Fig. 2, which shows side cross-sectional views (i.e., side views of the section shown in the inset of Fig. 1) of the melt pressure contours, liquid fraction contours and feeding flow velocity vectors and when solidification is 80% complete. The liquid fraction in the center of the plate at this point is around 40%, and the difficulty in feeding metal through this mushy zone creates a significant pressure drop. Once the plate freezes off, the hot spot region must solidify without feed metal, which causes a large region of macroshrinkage to form in the hot spot. This can be seen in Fig. 3, which illustrates the final pore volume percentages in the casting; also note the realistically predicted riser pipe. Finally, this plate exceeds the feeding distance by about 50%, and thus one would expect to see porosity in the plate as well. Fig. 4 shows the pore volume percentages in the plate, using a different scale than Fig. 3. The cross-sectional views shown in Fig. 4 demonstrate that there is, in fact, up to about 3% porosity in the center of the plate. This example aptly demonstrates the ability of the current model to predict porosity ranging from microporosity to large shrinkage cavities.

Interestingly, if this same casting is simulated without the block that causes the hot spot (i.e., just an end-risered plate), the maximum porosity in the center of the plate is about 9%. The lower amount of porosity in the plate with the hot spot block can be explained with the aid of Fig. 5,
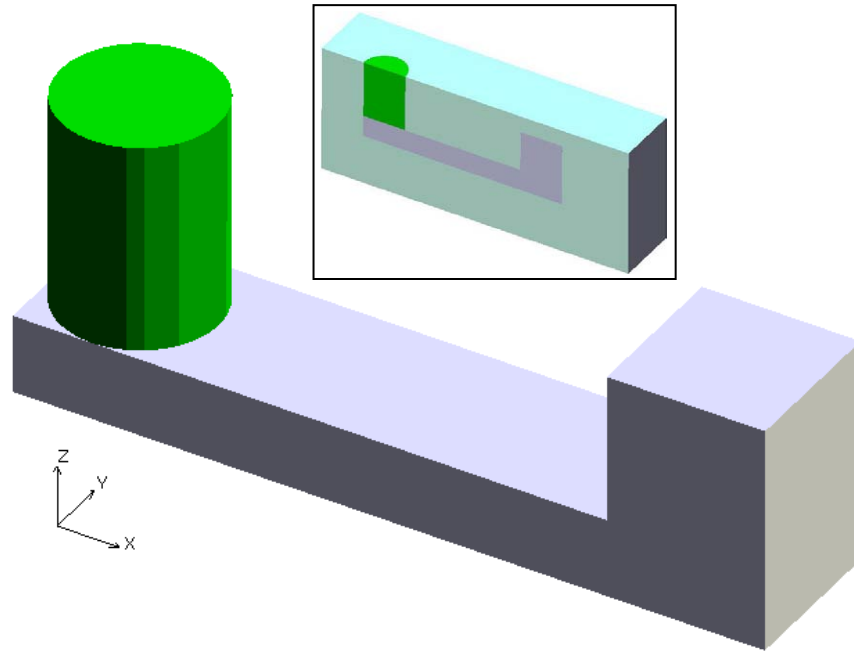
Figure 1. Casting geometry for the hot spot application, with an inset showing a side cross-sectional view that includes the mold.
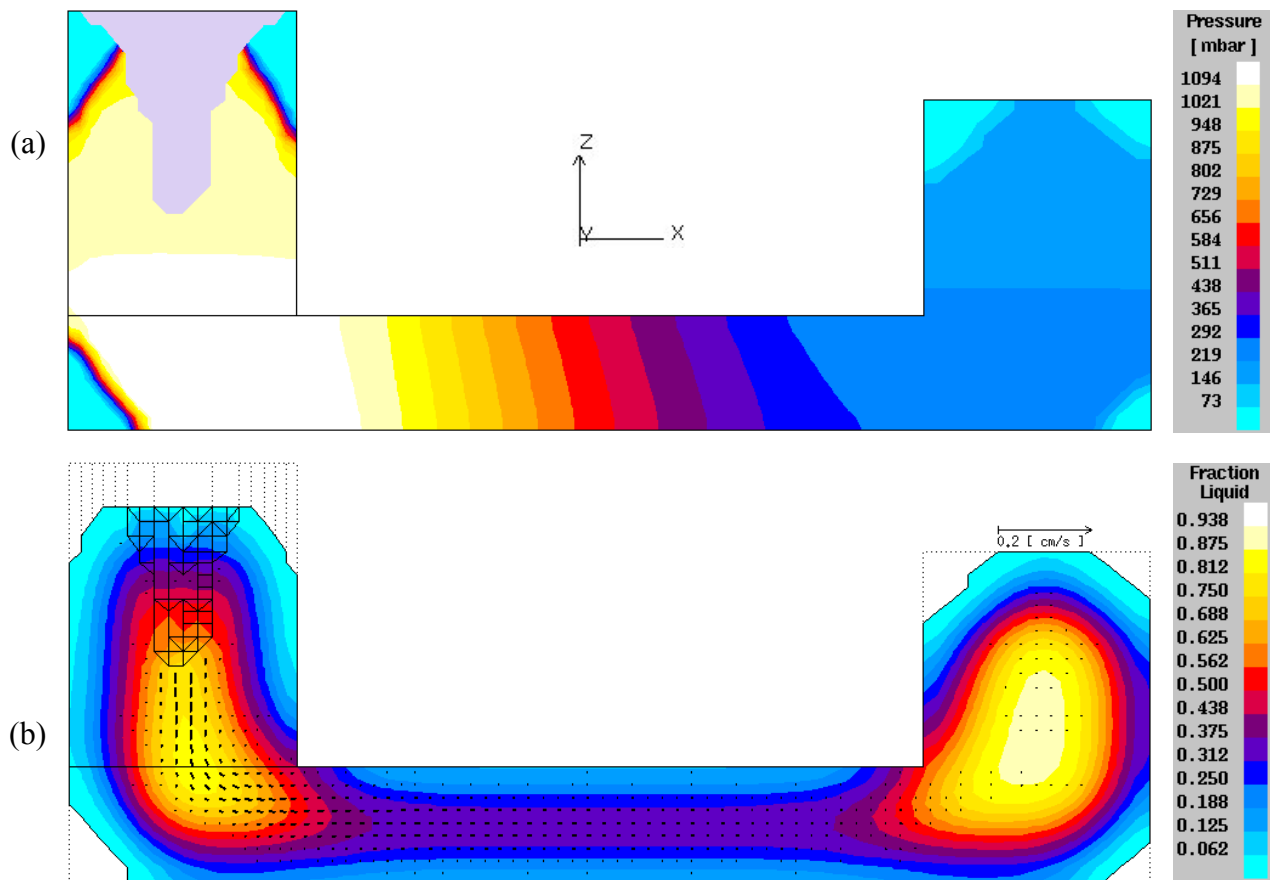

Figure 2. Side cross-sectional views of (a) melt pressure contours and (b) feeding flow vectors and liquid fraction contours, when the casting is 80% solidified.
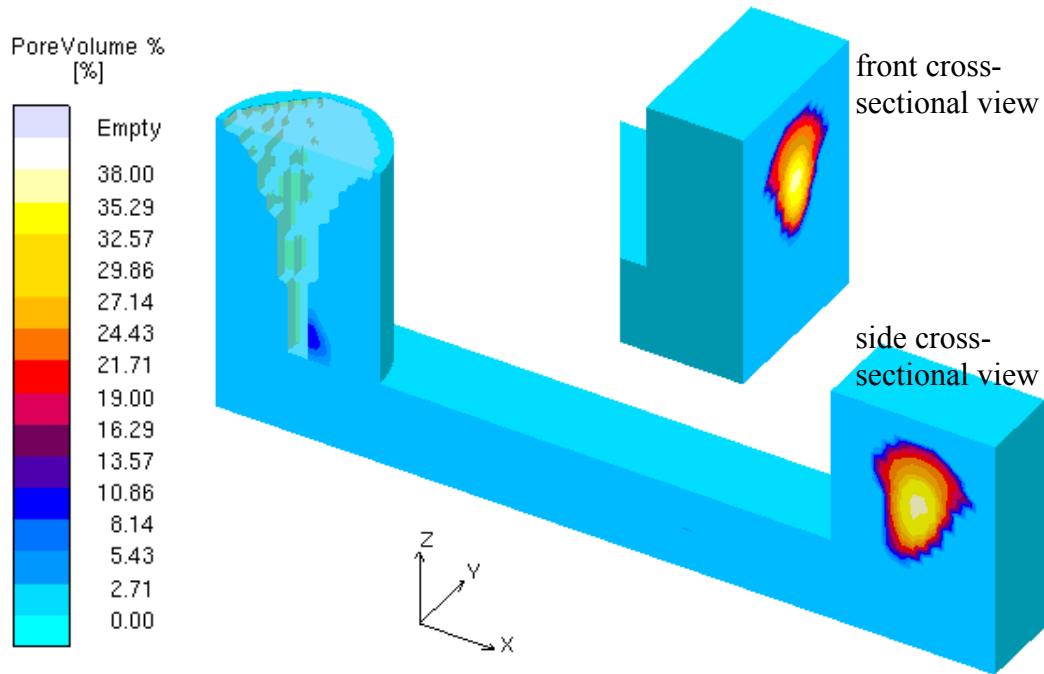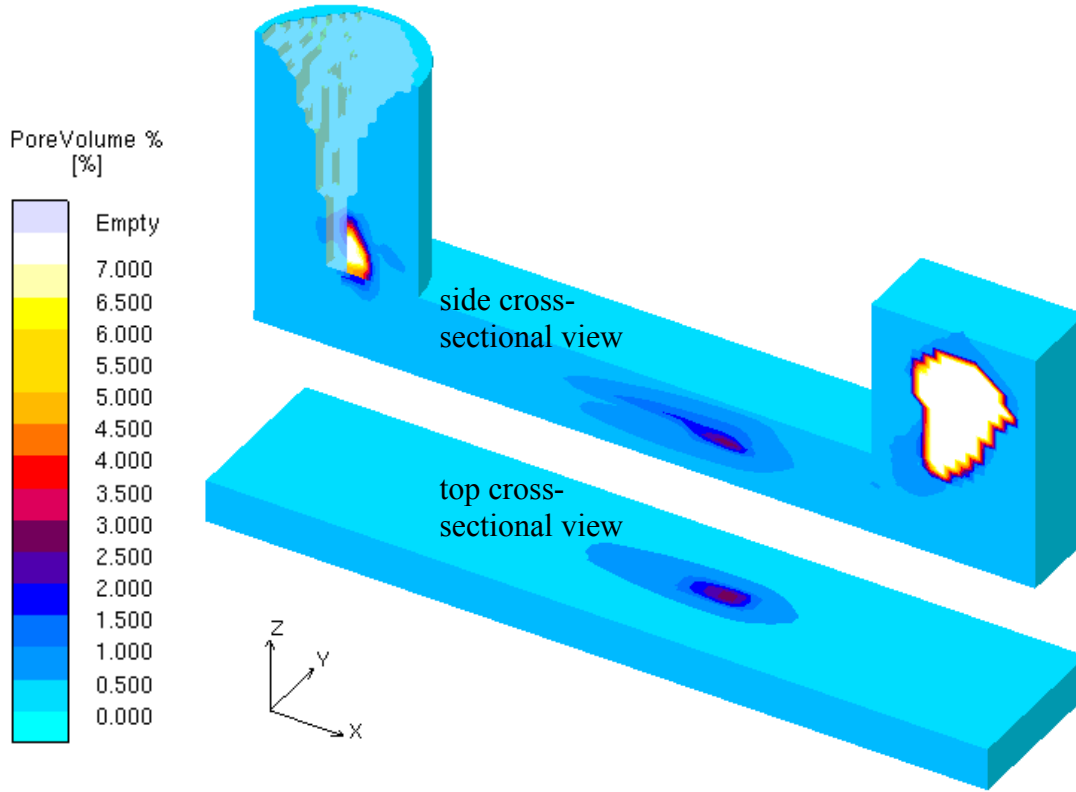
Figure 3. Final pore volume percentages in the hot spot.

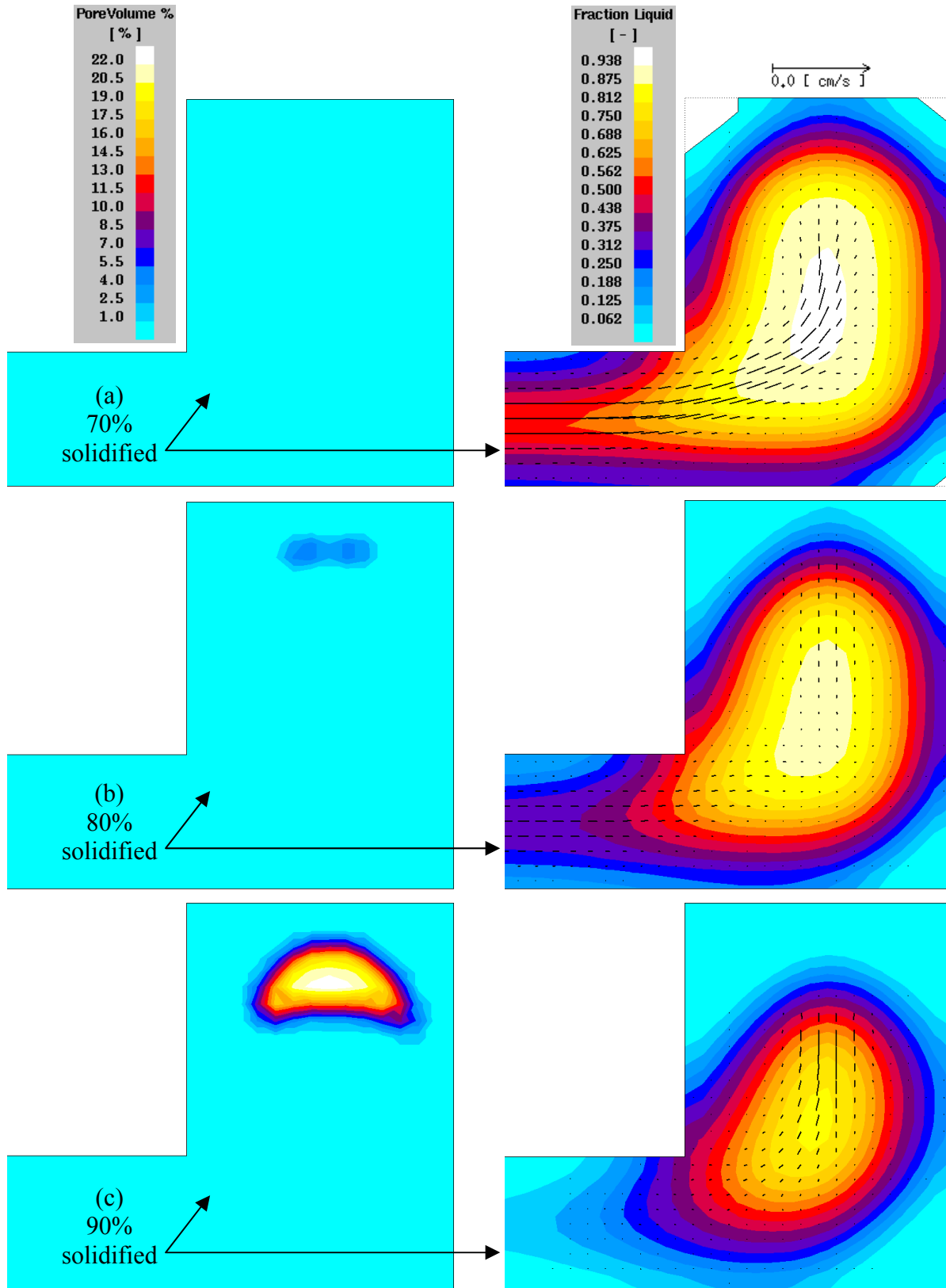

Figure 4. Final pore volume percentages in the plate.

Figure 5. Close-up side cross-sectional views of the hot spot area when solidification is (a) 70%, (b) 80% and (c) 90% complete, showing how the hot spot provides feed metal to the plate.

which shows side cross-sectional views of the hot spot area at various stages of solidification. Fig. 5a shows porosity percentage contours, liquid fraction contours and feeding flow vectors in the casting when it is 70% solidified. At this point, there is no significant porosity in the hot spot, and feeding flow progresses from the plate all the way up to the top of the hot spot. When the casting is 80% solidified (Fig. 5b), some porosity has nucleated near the top of the hot spot. The feeding flow from the plate is still flowing into the bottom of the hot spot, but now the hot spot is also being fed from above, by the region where porosity is forming. In essence, as porosity forms, it displaces liquid metal, which then flows downward to feed the hot spot. Some time after the situation depicted in Fig. 5b, the liquid fraction in the center of the plate drops low enough that the mushy zone becomes too impermeable to feed from the riser down the length of the plate, and the feeding flow moving from left to right in the plate ceases. Once this happens, the feeding flow in the hot spot area originates solely from the region where porosity is forming and growing. As shown in Fig. 5c, this feeding flow then feeds down into the hot spot, as well as into the end of the plate. Thus, with the hot spot block, the plate is supplied with feed metal longer than for a simple end-risered plate, and the porosity levels are lower in the plate cast with the hot spot block.

Test Specimen Castings

As part of a study of fatigue in cast materials containing porosity, fatigue test specimens were cast using the rigging arrangement shown in Fig. 6. A radiograph of the resulting castings is shown in Fig. 7a. As seen in these figures, traditional fatigue specimens were cast (#7 and #8), as well as a thin rod (#6), and rods having discs of varying thickness at their centers (#1 and #2 have thin discs, #3 has a thick disc, and #4 and #5 have an intermediate thickness). Each of these specimens has a minimum diameter of 9/16". Due to the small hot spot each disc creates during solidification, adding these discs creates macroporosity in the specimens. Discs of different
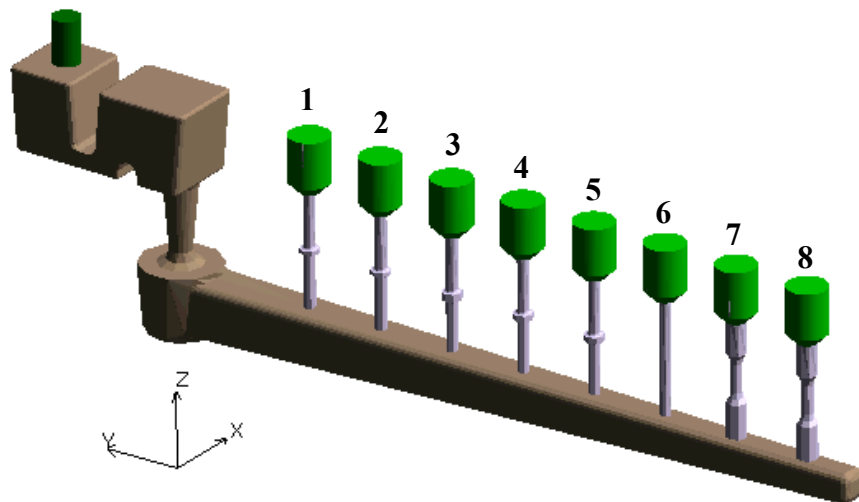

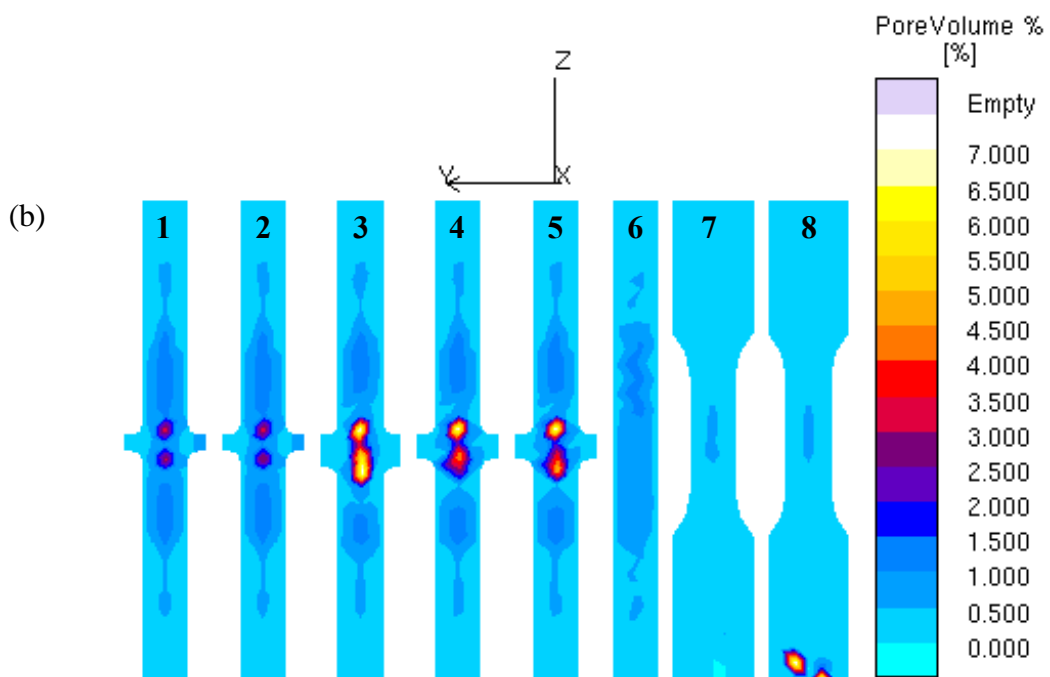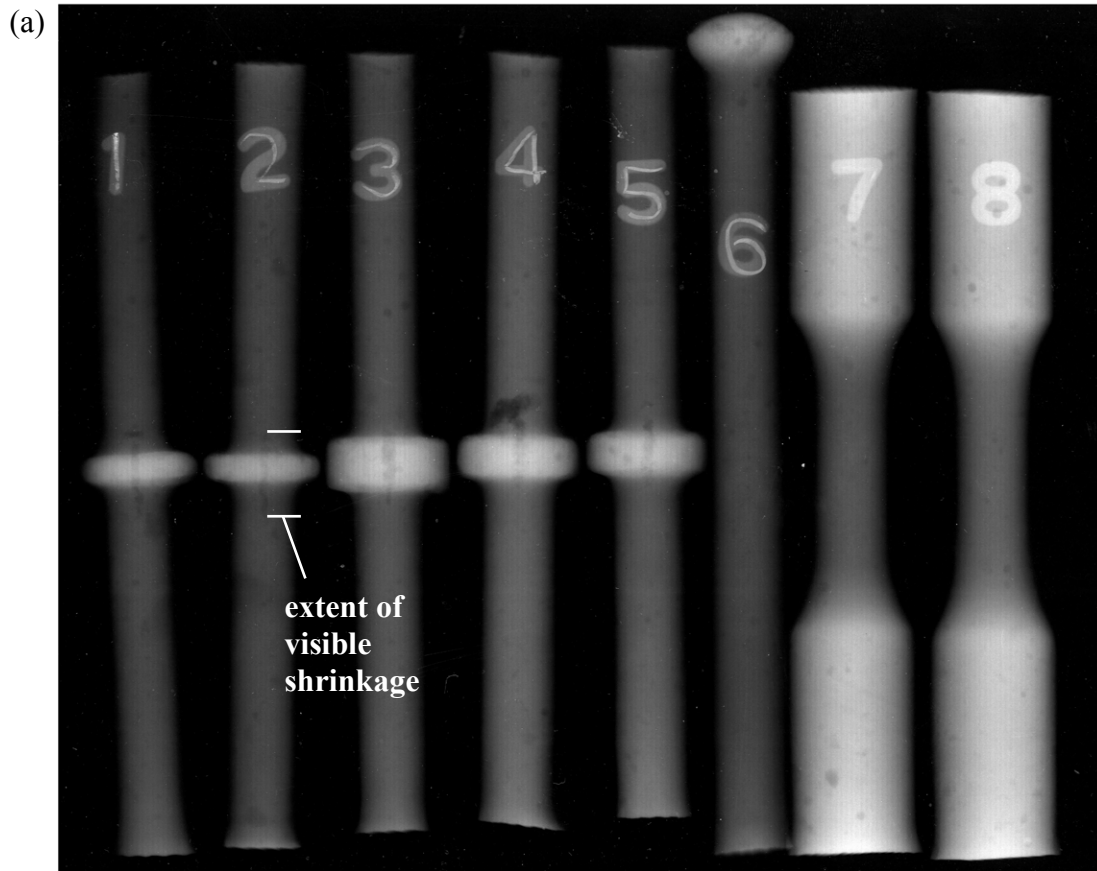
Figure 6. Rigging system for test specimen castings.

Figure 7. Comparison between (a) a radiograph of cast specimens and (b) simulated porosity percentages for the specimens.

thickness were used to create various levels of macroporosity. This is evident from the radiograph of specimens #1 - #5 in Fig. 7a. Specimen #3 has the largest amount of macroporosity, #4 and #5 have somewhat less, and #1 and #2 have the smallest amount of visible porosity. The shrinkage in #4 surfaced as a blowhole, which is visible in Fig. 7a. Specimens #6 - #8 show no visible shrinkage porosity. The simulation of this casting process included filling (at 2871°F) through the inlet, which is shown on the far left side of Fig. 6. The resulting pore volume percentages of the specimens are given in Fig. 7b. The simulation is in good agreement with the casting results in terms of both porosity location and relative amount; the largest amount of porosity appears in specimen #3, somewhat less porosity in #4 and #5, and less still in #1 and #2. Although specimens #6 - #8 were radiographically sound, each of them has indications of microporosity. More quantitative comparisons are currently underway.

Pressurized Riser Castings

Increasing feeding distances and improving casting soundness by pressurizing castings during solidification was investigated in a recent experimental study. The castings were pressurized by pressurizing the top of the riser. The trials were performed with 3"T x 6"W x 50"L plates, cast with the rigging shown in Fig. 8. The observation riser in this figure was necessary in order to determine when the casting was filled, because the metal could not be seen in the riser that was to be pressurized. Complete details regarding the pressurized riser study can be found in [9]. The study found that pressurizing the casting during solidification can significantly improve casting soundness. These casting trials were simulated using the present model. The simulation was performed without filling, with an initial temperature of 2840°F. Two simulations were performed: a base case without pressurization, and a simulation where a gage pressure of 5 bar was applied to the top of the pressurized riser. The final pore volume percentages for the non-pressurized and pressurized riser cases are shown in Fig. 9. As was found in the casting trials,
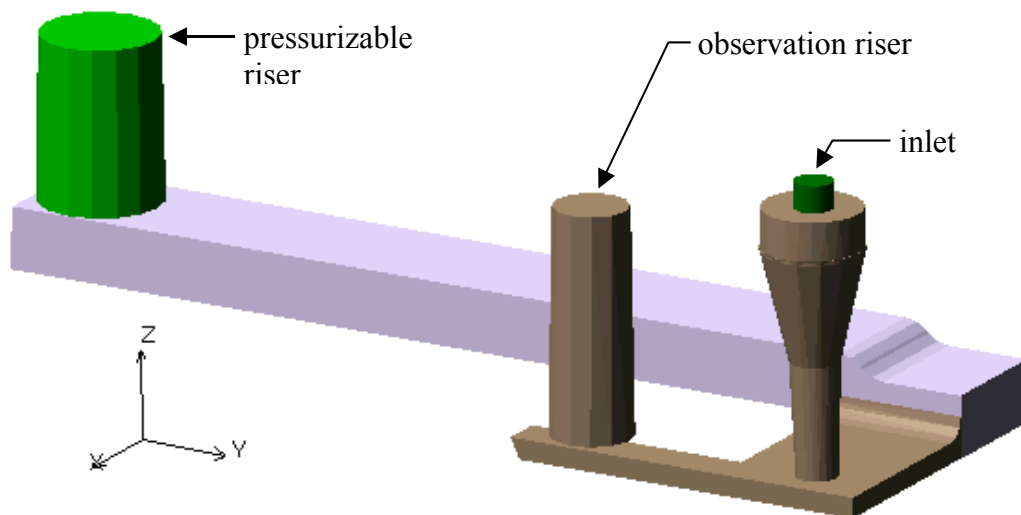

Figure 8. Rigging for pressurized riser casting trials.

pressurizing the riser significantly reduces the amount of porosity that forms in the castings. Figs. 10a and 10b provide a comparison between the casting trial radiographs and the simulation results for the non-pressurized and pressurized cases, respectively. Good qualitative agreement is seen. In particular, the simulation nicely reproduces the narrow band of centerline porosity in
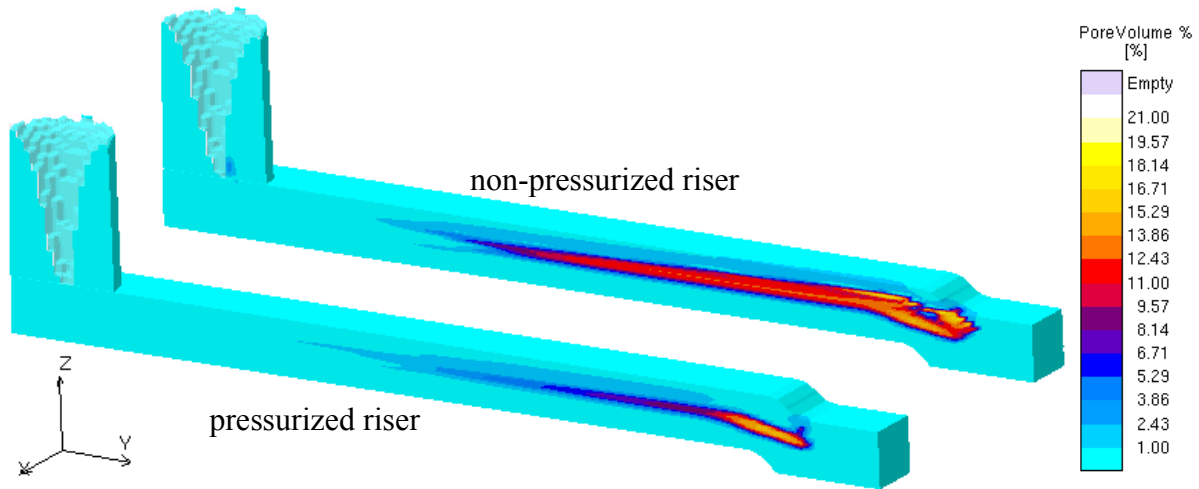

Figure 9. Final pore volume percentages in the middle of the plates, with and without pressurization.
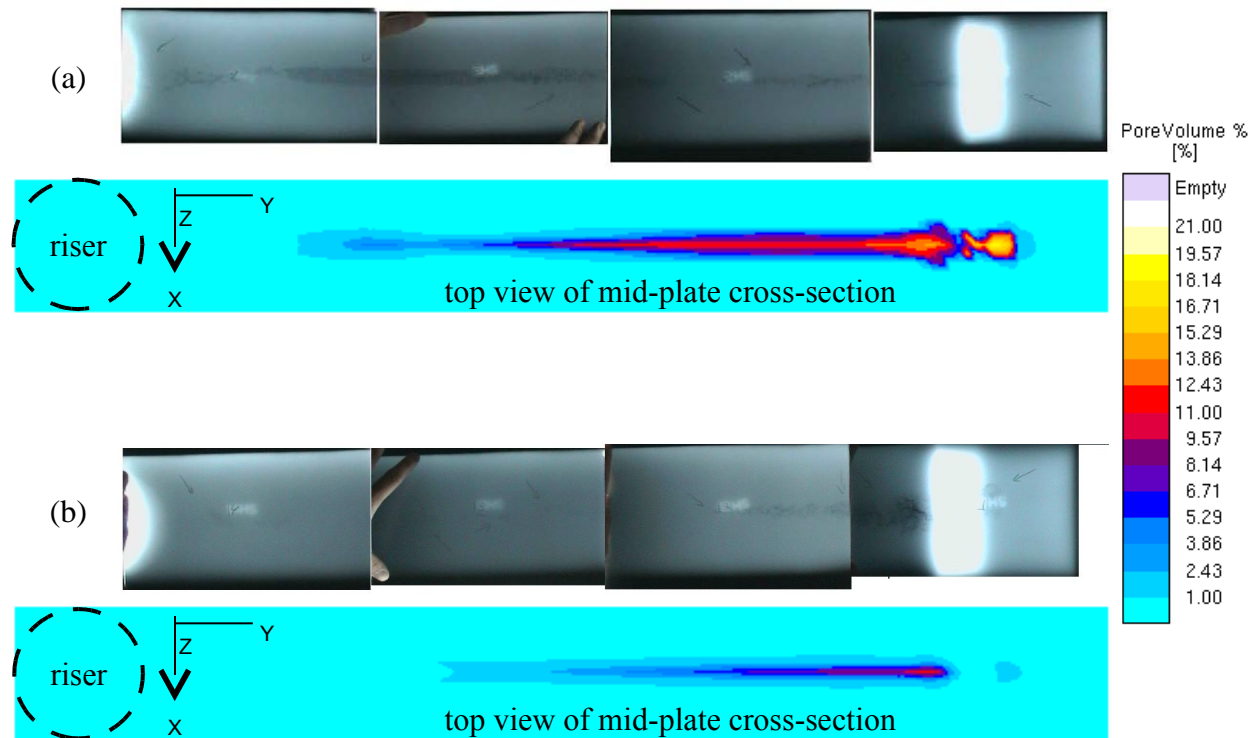

Figure 10. Comparison between radiographs and simulation results for (a) a non-pressurized casting, and (b) a pressurized casting.

the plate. However, the visible porosity on the non-pressurized casting radiograph in Fig. 10a extends closer to the riser than in the simulation result, and the porosity region in the pressurized casting radiograph in Fig. 10b is shorter than seen in the simulation result. In addition, it is worth noting that the maximum pressure applied in the casting trials was only 2 bar gage. The differences in the simulation results and the casting trials are likely due to several factors, including unknown gas levels in the casting trials, uncertainties in the permeability, and the fact that the simulations did not include filling. Still, the simulation results qualitatively capture the phenomena seen in the casting trials.

Conclusions

Using the governing equations underlying the physics of porosity formation, a multi-phase model was developed that predicts feeding flow, melt pressure, and the formation and growth of porosity in solidifying castings. The present model is valid for both microporosity and macroporosity, and is capable of predicting both shrinkage cavities and riser pipes as well. Applications were provided that demonstrated the ability of the model to predict large ranges of porosity in steel castings, and reasonable agreement was found with available experimental results. Additional parametric and validation studies are currently underway.

Appendix

In addition to the porosity defect modeling work just presented, the authors are also in the process of developing a model to predict reoxidation inclusion defects. The removal of inclusions from castings and the subsequent repair of those castings are expensive and time consuming procedures. Inclusions that remain in the casting adversely affect machining and mechanical performance, and may cause the casting to be rejected for failing to meet the radiographic standard requirements specified by the customer regarding allowable inclusion severity. It is intended that the model being developed will predict the formation of reoxidation inclusions during the pouring of steel castings, the advection and buoyant movement of these inclusions, and their final characteristics (composition, size, number density, etc.) and location in the solidified casting. The inclusion modeling project is in the first year of a three-year effort. Several areas of research are currently being pursued, namely inclusion formation, calculation of air entrainment, and mass particle tracking. The purpose of this appendix is to summarize the preliminary work done to date in these areas.

Formation. The precipitation of oxide inclusion particles out of the melt during steel casting, as well as the composition of these particles, can be determined by performing thermodynamic equilibrium calculations. This requires knowledge of the temperature and pressure, as well as the composition of the steel and dissolved gases, throughout the casting. Several commercial software packages are available that can perform the necessary thermodynamic equilibrium

calculations. The authors have recently obtained a license for one such package, Thermo-Calc [10], and are currently in the process of exploring its capabilities and limitations.

Air Entrainment. During the casting process, air can be entrained at all stages of filling: as metal flows from the ladle, into the pouring cup, down the sprue, through the gating, and into the casting. Although it has not been quantified, it is recognized that there is a correlation between air entrainment and the quantity of reoxidation inclusions that result in a casting [11]. Thus, if one reduces the amount of air that is entrained during filling, one should see a corresponding decrease in reoxidation inclusions. The role of air entrainment in reoxidation inclusion formation is currently being investigated by simulating two-phase flow (air and liquid). This is done using the Los Alamos National Laboratory multiphase fluid flow and solidification code Truchas.

As an example of a water modeling air entrainment simulation, consider filling of the simple two-dimensional basin shown in Fig. A1. This basin has a constant 80 cm^2/s water flow rate entering at the top right, a section adjacent to the water inflow area that is open to the atmosphere (called the air inlet), and another area open to the atmosphere on the top left (called the air outlet). Plots of the liquid free surface and velocity vectors in the liquid and air for various times during the filling process are given in Fig. A2, which shows results for a 34 x 68 grid. As the water stream enters the basin, it quickly contracts toward the wall. In order to conserve mass, the fluid flowing down the wall accelerates, and the velocity in this contracted region is considerably larger than the inlet velocity. This contraction effect is somewhat exaggerated, because the problem was solved with slip boundary conditions along the walls. Therefore, the fluid velocity along the walls can become large, and the entering water stream can become very narrow. In terms of air entrainment, notice that throughout the filling process, a considerable amount of air becomes encompassed by liquid, which creates air pockets within the water. Also notice that the

4 cm air inlet water inlet, uniform velocity of 20 cm/s (i.e., flow rate = 80 cm^2/s)
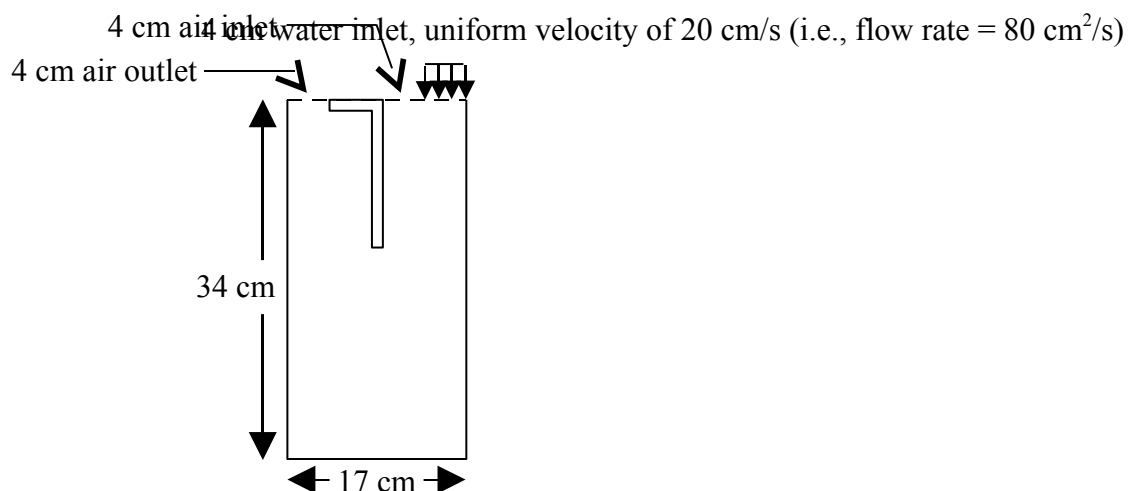
4 cm air outlet

34 cm

17 cm

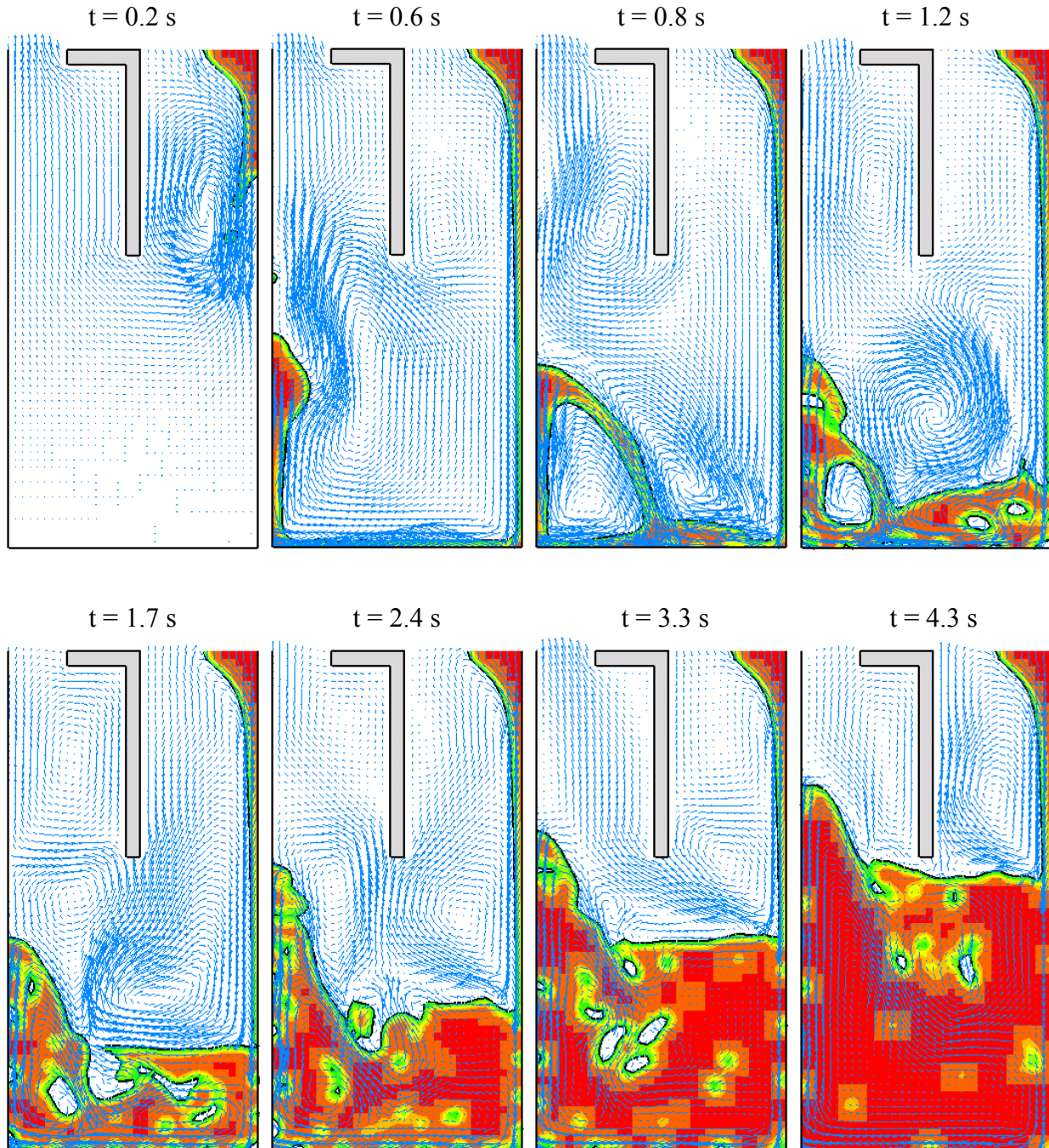Figure A1. Geometry for the two-dimensional air entrainment simulation.

Figure A2. Visualization of the velocity vectors and fluid surfaces at various times for the two-dimensional air entrainment simulation. These results are for a 34 x 68 grid.

area adjacent to the water inlet, termed the air inlet, actually has air flowing out of it during part of the filling process (see the results for t = 1.7 s, 2.4 s and 4.3 s). This figure demonstrates the complex nature of air entrainment, even for this simple two-dimensional filling problem.

Particle Tracking. Once inclusions have formed, it is then necessary to track their movement

through the gating and casting, in order to determine their final location. The present work in this area is being developed in Truchas as well as in MAGMASOFT. Both of these software packages were already capable of calculating the motion of massless particles. Massless particle tracking is relatively simple, since one merely moves each particle using the flow field velocity interpolated to the particle's present position. In other words, the particle velocity, $\mathbf{v}_p$, is equal to the liquid velocity, $\mathbf{v}_l$, at that location. To track particles with mass, it is necessary to include the effects of buoyancy, drag, etc. on the particle. The equation of motion for the particle is then given by

$$m_p \frac{d\mathbf{v}_p}{dt} = F_{drag} + F_{buoyancy} + F_{other} \qquad (A1)$$

where m_p is the mass of the particle, and F_{other} is a force term that accounts for added mass and pressure effects. The right-hand side of Eq. (A1) is a function of the velocity and thermophysical properties of the liquid, as well as the particle density, particle size, gravity, etc.

Consider an application that demonstrates the usefulness of such a mass particle tracking model. Fig. A3(a) shows the original rigging for a 3"T x 12"W plate cast during the University of Iowa/ SFSA low alloy steel plate casting trials [12], and Fig. A3(b) shows the resulting casting. Notice the large number of surface cavities (gas, inclusion or dross-related defects) on the cope surface of the casting. The revised rigging is shown in Fig. A4(a). In this rigging, the foundry switched from the thin, flat runners that were used in the original design to a cylindrical downsprue and runner system, in which the metal exits the gating and enters the casting by pouring up into the risers. The cope surfaces of the resulting castings were much cleaner, as seen in Fig. A4(b). Filling was simulated for both of these rigging designs, releasing mass particles in the downsprue and tracking their motion throughout the casting. The particles were assigned a diameter of 100 microns and a density of 3400 kg/m^3 (representative of Al$_2$O$_3$, a very common constituent of inclusion particles in steel). A low-alloy steel was used for the simulation, so the inclusion particles are about half as dense as the liquid metal. An illustration of these particle simulations during the filling process is provided in Fig. A5, which shows particle locations about halfway through the filling process. Fig. A5(a) is from the original rigging, while Fig. A5(b) is from the revised rigging. In Fig. A5(a), notice that the particles enter the plate through each ingate, and turn toward the center of the plate as they near the side of the plate opposite the gating. The two streams of particles (one stream from each ingate) then meet near the center of the plate on the side opposite the gating, and are forced to turn into the middle of the casting. This forms two regions of recirculating flow (i.e., vortices) in the casting; these vortices hold the particles in the plate, which results in the dirty cope surface seen in Fig. A3(b). With the revised rigging, however, Fig. A5(b) shows that the particles flow out of the gating system into the risers, and many of the particles stay in the risers. There are particles in the plate, but a significantly smaller

number of them.   And   the   particles   in   the   plate   are   not   being   held   there   by
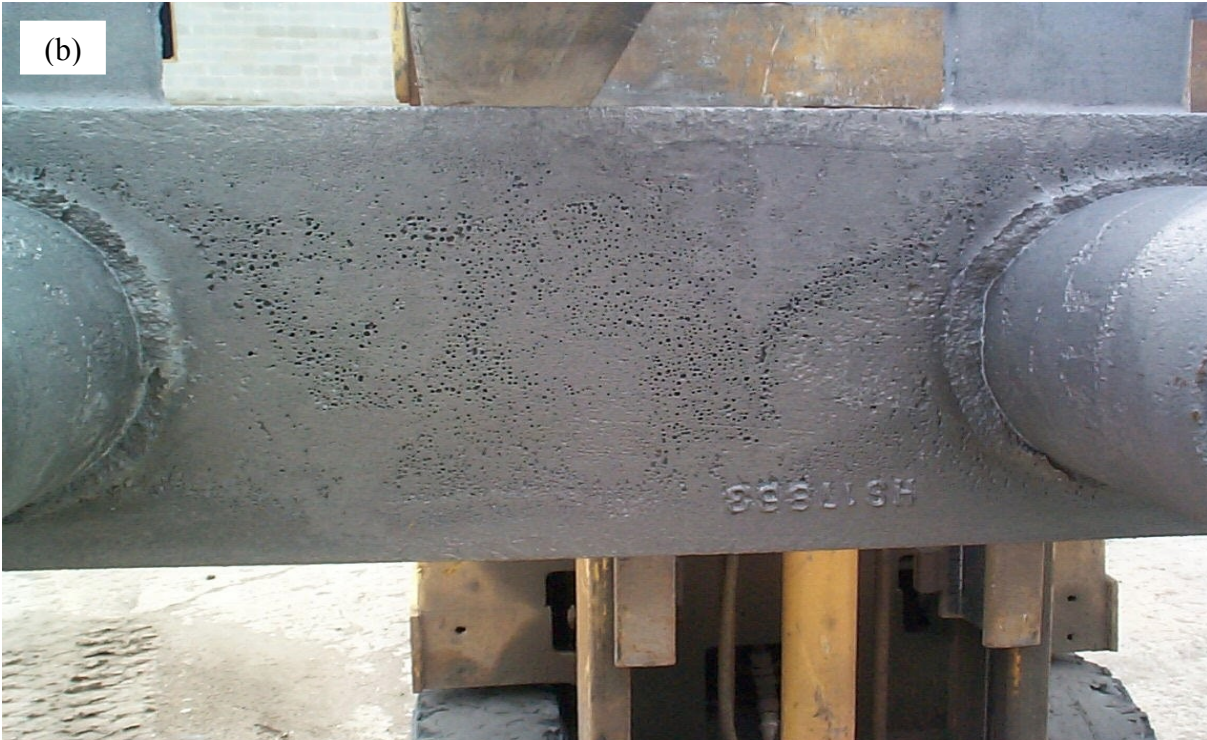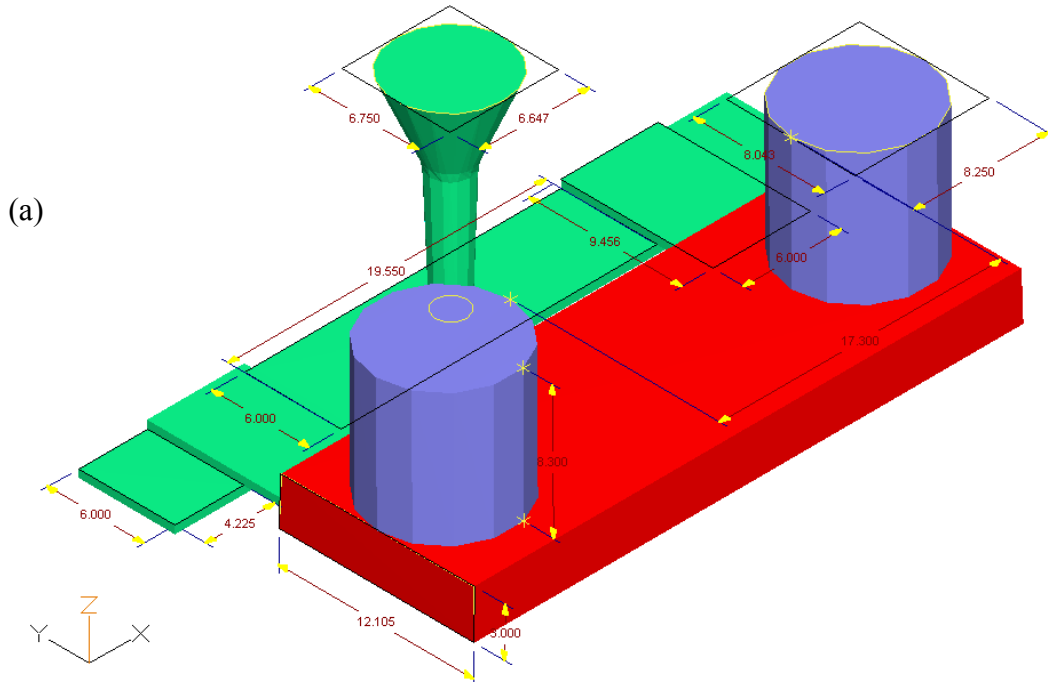
Figure A3. (a) Schematic of the original rigging design (dimensions are in inches), and (b) a picture of the cope surface cavities that resulted from this rigging.
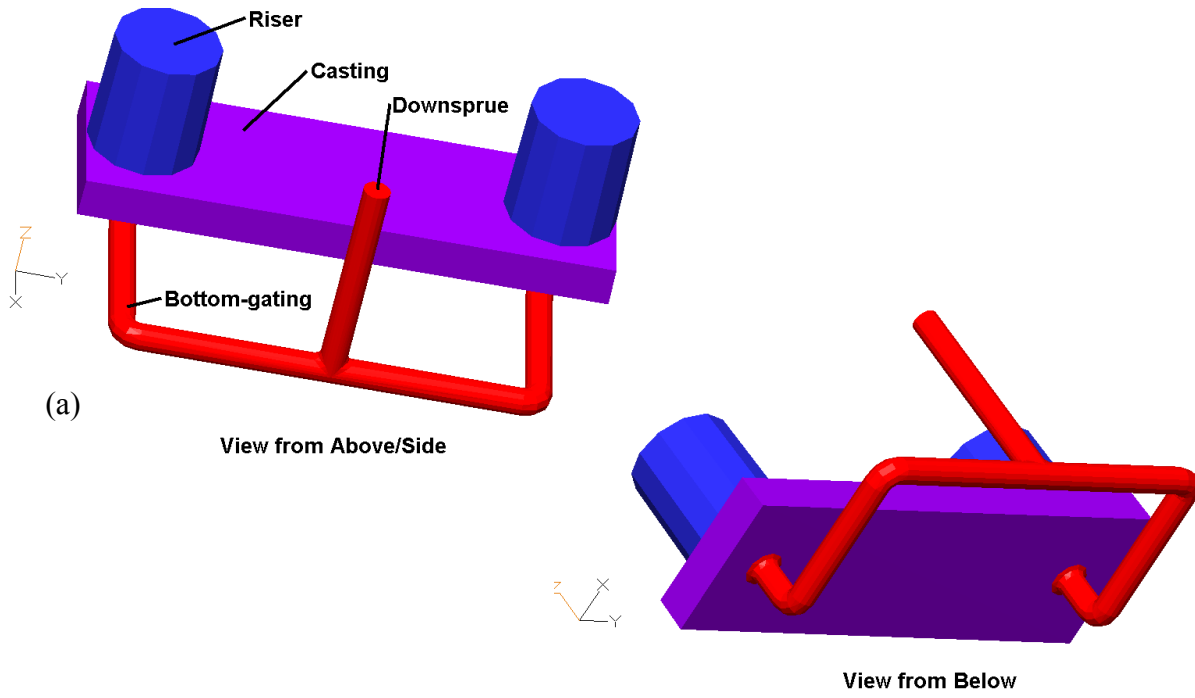
Figure A4. (a) Schematic of the revised rigging design, and (b) a picture of the clean cope surface resulting from this rigging.
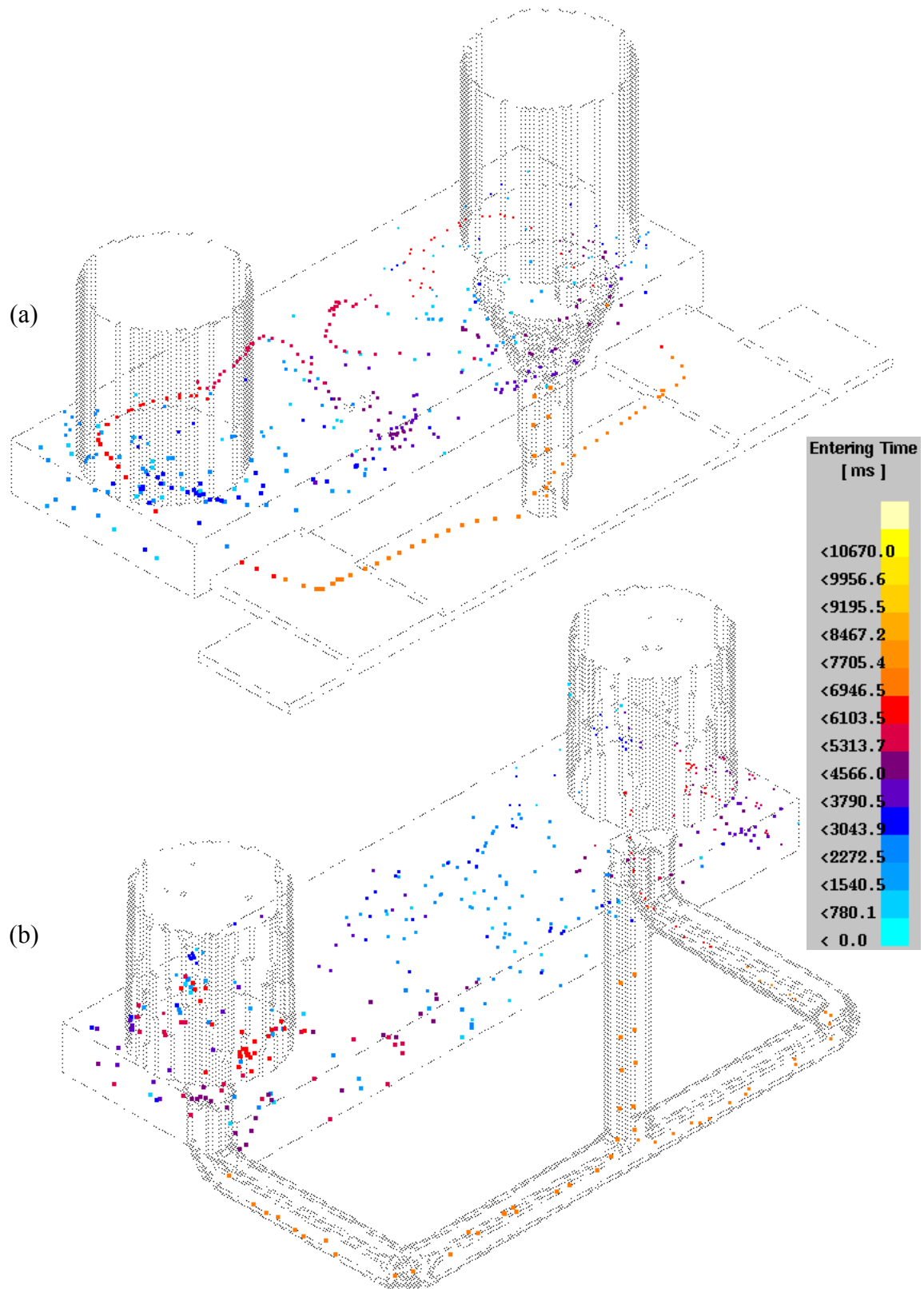
Figure A5. Mass particle tracking results for (a) the original rigging and (b) the revised rigging, about 7 seconds into the filling process.

recirculation regions, so many of the particles in the plate will eventually end up in the risers as well. This results in the cleaner cope surface seen in Fig. A4(b).

Acknowledgements

References

[1] T.S. Piwonka and M.C. Flemings, "Pore Formation in Solidification," <u>Trans. AIME</u>, 236 (1966), 1157-1165.

[2] K. Kubo and R.D. Pehlke, "Mathematical Modeling of Porosity Formation in Solidification," <u>Metall. Trans. B</u>, 16B (1985), 359-366.

[3] P.D. Lee, A. Chirazi, and D. See, "Modeling Microporosity in Aluminum-Silicon Alloys: A Review", <u>J. Light Metals</u>, 1 (2001), 15-30.

[4] A.S. Sabau and S. Viswanathan, "Microporosity Prediction in Aluminum Alloy Castings," <u>Metall. Mater. Trans. B</u>, 33B (2002), 243-255.

[5] Ch. Pequet., M. Gremaud, and M. Rappaz, "Modeling of Microporosity, Macroporosity, and Pipe-Shrinkage Formation during the Solidification of Alloys Using a Mushy-Zone Refinement Method: Applications to Aluminum Alloys," <u>Metall. Mater. Trans. A</u>, 33A (2002), 2095-2106.

[6] C.Y. Wang and C. Beckermann, "A Two-Phase Mixture Model of Liquid-Gas Flow and Heat Transfer in Capillary Porous Media—I. Formulation," <u>Int. J. Heat Mass Transfer</u>, 36 (11) (1993), 2747-2758.

[7] *MAGMASOFT*, MAGMA GmbH, Kackerstrasse 11, 52072 Aachen, Germany.

[8] J. Miettinen, "Calculation of Solidification-Related Thermophysical Properties for Steels," <u>Metall. Trans. B</u>, 28B (1997), 281-297.

[9] R.A. Hardin, T. Hays, and C. Beckermann, "Pressurized Riser Casting Trials" (Paper presented at the 55th Steel Founders' Society of America Technical and Operating Conference, Chicago, Illinois, 2 November 2001).

[10] *Thermo-Calc*, Thermo-Calc Software, Stockholm Technology Park, Björnnäsvägen 21, SE-113 47 Stockholm, Sweden.

[11] J.A Griffin and C.E. Bates, "Ladle Treating, Pouring and Gating for the Production of Clean Steel Castings," Steel Founders' Society of America Research Report No. 104, Technical Steering Committee Report (1991).

[12] R.A. Hardin, S. Ou, K. Carlson, and C. Beckermann, "Relationship Between Casting Simulation and Radiographic Testing: Results from the SFSA Plate Casting Trials" (Paper presented at the 53rd Steel Founders' Society of America Technical and Operating Conference, Chicago, Illinois, 5 November 1999).